RESEARCH PAPER

Enhancement of the ozone-sensing properties of ZnO through chemical-etched surface texturing

Weverton A. dos Santos Silva ⓘ ·
Bruno S. de Lima · Maria I. B. Bernardi ·
Valmor R. Mastelaro

Abstract Semiconductor metal oxides (SMOx) are widely studied for different applications. It is well established that the gas-SMOx interaction strongly depends on the charge exchange between the exposed surface area and the target gas. Hence, nanostructuring processes can amplify these surface effects and enhance SMOx sensitivity. Recently, different studies have demonstrated that nanostructured ZnO-based devices exhibit improved efficiency by chemical etched surface texturing using diluted hydrochloric acid (HCl) solutions. In this context, this study investigates the influence of chemical etching by HCl on the gas-sensing properties of ZnO thin films regarding ozone (O_3) detection. The X-ray photoelectron spectroscopy analysis suggested an increase in the density of surface defects in the etched samples, leading to a higher density of adsorption sites for gas molecules. Scanning electron microscopy images before and after acid immersion revealed an increase in the surface area as the average grain size decreases and the film's porosity increases. Measurements of the gas-sensing properties operating at 300 °C showed that the nanostructuring process significantly enhances the sensitivity of ZnO thin films for O_3 detection, indicating

a synergic effect between the grain size decrease and the porosity increase. Our results demonstrate that this methodology can be used to enhance the sensitivity of SMOx-based gas sensors.

Keywords Thin films · ZnO · Chemical etching · HCl · Ozone · Gas sensor · Nanostructure · Semiconductor metal oxides

W. A. dos Santos Silva (✉) · B. S. de Lima ·
M. I. B. Bernardi · V. R. Mastelaro
São Carlos Institute of Physics, University of São Paulo,
São Carlos, SP, Brazil
e-mail: wevertonalison@gmail.com

Introduction

Zinc oxide (ZnO) is a semiconductor with striking characteristics from a scientific and technological perspective due to its bandgap of 3.3 eV, chemical and thermal stability, and nontoxicity (Hu et al. 2018; Dey 2018). This material is well-known for its versatility, as it can be obtained in different morphologies, such as nanowires (Aisida et al. 2019), nanobelts (Barnard et al. 2006), nanotubes (Kong et al. 2004), and nanorods (Aisida et al. 2020), among others (Goldberger et al. 2005; Mahmud et al. 2006; Matsuoka 1971). It can be prepared by various techniques, including hydrothermal synthesis (Savu et al. 2009), polymeric percussion (Catto et al. 2014), and sputtering (Colmenares et al. 2020). This semiconductor metal oxide (SMOx) has been explored for applications in gas-sensing devices, light-emitting diodes (LEDs), and solar cells, among others (Ji and Ye 2008; Zhu and Zeng 2017). When synthesized, ZnO crystallizes in the hexagonal structure known as

wurtzite and exhibits n-type conductivity due to point defects in its structure (McCluskey and Jokela 2009).

Since the pioneering work by Seiyama et al. in 1962 (Seiyama et al. 1962), sensors based on zinc oxide have been used to detect reducing (i.e., H_2, CO, and NH_3) and oxidizing (i.e., NO_2, CO_2, and O_3) gases. The gas detection mechanism of such materials is based upon the surface adsorption and desorption of ionic species from the gas through redox reactions. When a ZnO-based sensor is exposed to an atmosphere that contains oxygen (O_2), some molecules are adsorbed to its surface by capturing electrons from its conduction band and forming a layer of negatively charged ions bonded to its surface. This process is called oxygen ionosorption (Sopiha et al. 2021), and its nature is fundamental to comprehending the sensing mechanism of a specific target gas. For instance, when ZnO is exposed to a reducing gas, the adsorbed oxygen ions will react with the gas, releasing electrons into the material, thus reducing the depletion layer and decreasing the electrical resistivity of the material (Barsan et al. 2007; Wang et al. 2010). For oxidizing gases, on the other hand, ionic species are adsorbed on the ZnO surface, leading to electron consumption and consequently increasing the depletion layer and its electrical resistivity. It can be noted that the material's surface area plays an important role in the performance of the material as a gas sensor since the higher the surface area, the more adsorption sites will be available for oxygen species to adsorb.

Different techniques aiming to increase the surface area of SMOx gas sensors and consequently decrease their operating temperature and increase their sensitivity have been studied. According to Korotcenkov (Korotcenkov 2008), the most critical parameters to increase the material's surface area are grain size, film thickness, and texture. Other techniques can be used to improve the performance of SMOx-based sensors, such as doping (McCluskey and Jokela 2009), UV activation (Luís et al. 2017), or heterojunction fabrication (Basyooni et al. 2017). Within this context, different studies have shown that chemical etching can also induce the formation of pores and decrease the grain size of nanostructured SMOx, leading to an increase in the surface area (Yan et al. 2015). Yan and collaborators (Yan et al. 2016) reported the increase of porosity through chemical etching on Al-doped ZnO thin films using hydrochloric acid diluted in deionized water at a volume concentration of 0.5%.

They observed a change in porosity according to the variation in immersion time in the acid. Owen and collaborators (Owen et al. 2011) performed a procedure using two solutions: hydrofluoric acid (1 v/v%) and hydrochloric acid (0.5 v/v%) solutions. The etching process was also carried out on Al-doped ZnO films deposited through RF magnetron sputtering using a metallic target. The authors concluded that this procedure induces a more homogeneous distribution of pores. Bunte et al. (Bunte et al. 2011) reported similar results for Al-doped ZnO films deposited through ceramic targets using the same methodology.

Here, we investigate the acid etching efficiency in modifying ZnO thin films ozone sensing properties. As mentioned before, it has already been shown that HCl etching can be used as an efficient technique to induce the formation of pores and decrease the grain size of the material since the etching reactions occur preferably in the grain boundaries (Shang et al. 2015). This technique has not been explored in SMOx thin films applied to gas sensors. In this work, ZnO thin films were deposited by RF magnetron sputtering and etched using HCl solutions. X-ray diffraction and Raman spectroscopy revealed that HCl etching has no impact on their crystal structure. Surface analysis through X-ray photoelectron spectroscopy (XPS) suggested an increase in the density of point defects in oxygen sites, which can be depicted as new adsorption sites for gaseous species. Scanning electron microscopy imagining showed that this methodology also induces the formation of pores. Finally, our results demonstrated that HCl etching increases the ZnO sensitivity and decreases its response and recovery time due to an increase in the porosity and surface area of the films.

Experimental procedure

ZnO deposition and HCl etching

ZnO films were deposited via RF magnetron sputtering using a 3-in target of pure metallic zinc 6.5 cm far from the Si/SiO_2 substrates operating at a radio frequency of 13.5 MHz and power of 60 W. The chamber was kept at a high vacuum (5×10^{-6} mbar) for 1 h before the deposition. The pressure inside the chamber was kept at 2.5×10^{-2} mbar with constant argon injection during

the deposition. Films with different thicknesses were obtained by varying the deposition time and keeping the other parameters fixed. After metallic zinc deposition, these films were heat-treated under air for 1 h at different times and temperatures to obtain thin single-phase zinc oxide films. The thickness of the films was determined on a Veeco Dektak 150 profilometer. The oxidized films were then inserted into a 2.75 mM HCl water solution. The solution was prepared by diluting concentrated HCl (37%v) in deionized water in the correct proportions. The etching process was controlled by monitoring the time of immersion. After etching, each sample was rinsed in deionized water and sonicated for 10 min to stop the reaction.

Thin-film characterization

The structural properties of ZnO films were analyzed using X-ray diffraction (Rigaku Diffractometer, Ultima IV) and Raman spectroscopy. The diffractograms were collected in the range from $2\theta = 20$ to $80°$ with a step of $0.02°$ at a scanning speed of $2°/min$. The X-ray was generated by a copper target ($\lambda = 1.5418$ Å) and a nickel filter. The diffraction patterns were analyzed with the General Structure Analysis System II (GSAS-II) software (Toby and Dreele 2013). The Raman spectra were obtained in a WITec microscope (Ulm, Germany) equipped with Nikon objectives (20x). The samples were excited using a continuous Ion Ar (514 nm) laser. The signal was collected by a CCD system cooled by a Peltier module and 0.5 cm^{-1} resolution. The spectrum was acquired at room temperature using a diffraction grid of 1800 lines per millimeter. The chemical composition and oxidation state of the elements present on the surface of the ZnO films were measured in a Scienta Omicron ESCA spectrometer with Al-Kα monochromatic X-ray source (1486.7 eV, with the power of 280 W and constant energy of 50 eV). The XPS spectra were adjusted using Shirley's background subtraction method, and the peaks were adjusted by mixed Gaussian–Lorentzian curves and a least-squares routine. The obtained spectra were corrected, assuming 284.8 eV for adventitious carbon. Scanning electron microscopy imaging was carried out using a Field-Emission Supra 35-VP Carl Zeiss. The images were

processed using ImageJ software (Rueden et al. 2017).

Gas-sensing performance

For the gas-sensing experiments, ZnO thin films were deposited onto Si/SiO_2 substrates containing 100-nm-thick Pt interdigitated electrodes. The electrical resistance of these films was continuously monitored by measuring the electrical current with a Keithley 6514 electrometer when an excitation voltage of 1 V was applied between the electrodes. The substrates were kept inside a sealed chamber containing a temperature PID controlled hot plate for precise temperature control, gas inlet, and outlet. For our experiments, the operating temperature was kept constant at 300 °C, and the air humidity constant at 20%. The ozone-controlled exposures were carried out by exposing the dry airflow to an ultraviolet lamp (UVP, model P/N 90–0004-01). A commercial ATI (model F12) electrochemical gas detector was used to determine the real concentration of ozone.

Results and discussions

Figure 1 shows the X-ray diffraction patterns of ZnO films by the procedure described in Sect. 2.1. The lower diffraction pattern (data in black) was obtained from a film after the deposition process. It is possible
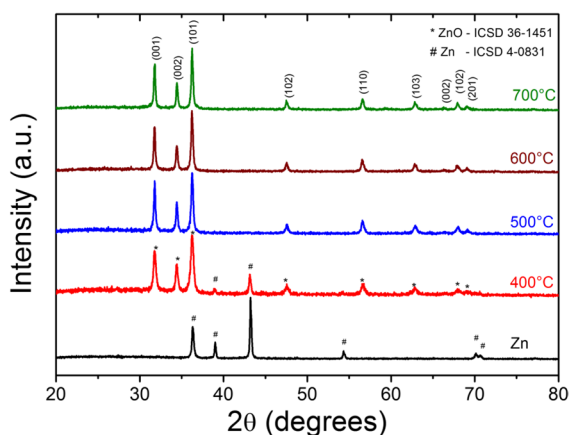

Fig. 1 XRD data of metallic Zn thin films heat-treated at different temperatures under air. It is possible to observe that the metallic zinc films are completely oxidized when the heat treatment is carried out at 500 °C or higher

to observe that the diffraction pattern only presents peaks related to the metallic Zn phase, with hexagonal crystal structure belonging to the $P6_3/mmc$ (194) spatial group (Nuss et al. 2010). After 1 h of heat treatment at 400 °C (data in red), peaks from both metallic Zn (marked with #) and ZnO (marked with *) can be seen, suggesting partial oxidation of the metallic film at this temperature. The ZnO phase peaks were indexed to the wurtzite structure, $P6_3mc$ (186) space group (Franco and Pessoni 2017). For treatments at temperatures higher than 500 °C, it was possible to obtain single-phase samples of ZnO. In other words, no trace of metallic zinc could be observed within the resolution of the XRD technique. Thus, 500 °C proved to be the lowest temperature required to obtain only crystalline ZnO films without the metallic secondary phase. It is worth emphasizing that this heat treatment is important for the thermal stability of the sensors since ZnO films for gas-sensing performance experiments are kept at 300 °C for several hours. The Rietveld refinement was carried out to analyze the structural evolution of ZnO films as a function of temperature. These results are shown in Table 1. As it can be seen, there is a significant increase in the crystallite size as the heat treatment temperature rises. For instance, it was 32 nm for the sample heat-treated at 400 °C and approximately 60 nm for higher temperatures. This increase in the crystallite size can be related to an increase in the average size of the grain structure, which may cause a degradation of the sensing properties of the films due to the decrease in their surface area.

To better understand the structural evolution as a function of temperature, the Raman spectrum was measured in the samples heat-treated at 500, 600, and 700 °C for 1 h. Figure 2 shows this dataset. The
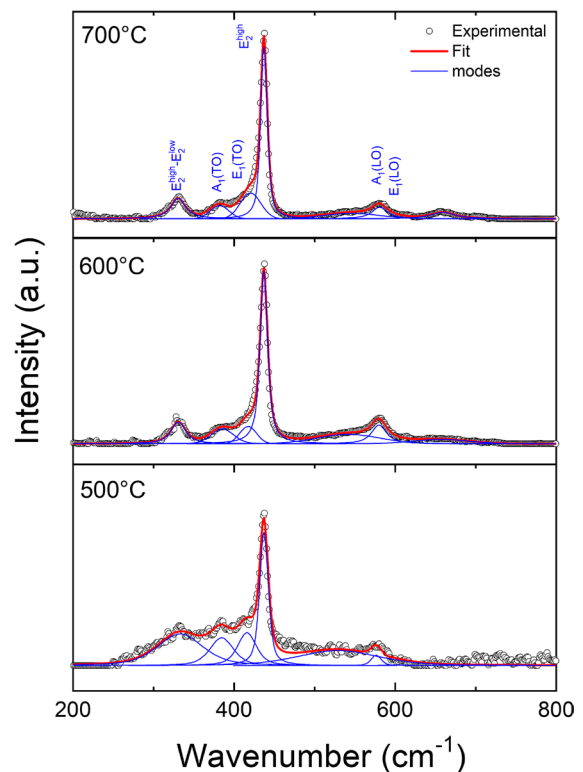

Fig. 2 Raman spectra evolution of ZnO. The figure shows six first-order peaks of the A1, E1, and E2 optical phonon modes. Peaks are well defined at higher temperatures, suggesting a more efficient crystallization process

Table 1 Rietveld refinement results of the diffractograms shown in Fig. 1

Heat-treatment temperature (°C)	a (Å)	c (Å)	Crystallite size (nm)	Residue	
				(R_{wp})	GOF
400*	3.251	5.211	32	19.1	1.10
500	3.251	5.210	59	18.5	1.16
600	3.253	5.210	59	17.1	1.13
700	3.252	5.206	60	19.2	1.17

*This sample is composed of 80.3 at.% of wurtzite ZnO and 19.7% of metallic Zn. The values on the table correspond to the ZnO wurtzite phase

spectrum was fitted using the vibration modes from the literature. According to Russo and collaborators (Russo et al. 2014), the Raman spectra of the wurtzite phase of ZnO exhibit six first-order peaks related to the modes of optical branches of A_1, E_1, and E_2. The two most intense peaks present in the ZnO spectra are in the vicinity of 99 and 438 cm^{-1}, resulting from Zn and O sublattices vibrations, E_2^{high} and E_2^{low}. A combination of these two modes (E_{2high}–E_{2low}) generates a small peak close to 330 cm^{-1}. Other important features found in the Raman spectrum can be noted at 391, 424, 437, 576, and 581 cm^{-1}, assigned to A_1 (TO), E_1 (TO), E_{2high}, A_1 (LO), and E_1 (LO), respectively (Russo et al. 2014; Zhang et al. 2009; Phan et al. 2008). The peaks observed at 523 and 660 cm^{-1} are related to second-order modes, frequently associated with specific point defects in the Zn and O sites (Cerqueira et al. 2015). It is possible to find in the literature small differences in the wavenumber attributed to the peaks observed in the Raman spectrum of

ZnO samples. According to Phan et al. (Phan et al. 2008), the ZnO Raman spectrum can undergo small displacements due to the different morphologies that ZnO can grow into. The intensity ratio of the E1(LO) in relation to the E_2^{low} is shown in Table 2 as a function of heat treatment in temperature. It is possible to observe a decrease in the relative intensity of the band centered at 581 cm^{-1}. As this band is associated with the longitudinal vibration of oxygen atoms, it must be susceptible to the presence of oxygen-related defects (Cerqueira et al. 2015), and also, for higher heat-treatment temperatures, the number of point defects is expected to diminish. This dataset is in agreement with the XRD data since both figures suggest an improvement in the film crystallinity.

Figure 3 shows the XPS data for the surface characterization of a ZnO thin film deposited under Ar and heat-treated under air at 500 °C for 1 h. Different etching times are investigated in this Figure. Figure 3(a) presents the survey spectra of these films, in which it is possible to observe peaks related to Zn 2p, O 1 s, and C 1 s (Ribeiro et al. 2019). The amount of each element was estimated for each sample, and the results are shown in Table 3. High-resolution measurements were carried out in the regions of Zn 2p (~1030 eV), O 1 s (~532 eV), and C 1 s (285 eV). The most significant differences were observed in the high-resolution XPS spectra of O 1 s as a function of etching time. The lower panel of Fig. 3 shows the high-resolution spectrum of each sample etched with HCl. This dataset indicates that etched samples exhibit higher peroxide content. According to Dubin et al. (Dupin et al. 2000), the component centered in 530 eV (in black) is related to structural O^{2-} ions. In contrast, the 532 eV component (in red) is frequently associated with the formation of peroxide defects with charge O$^-$ (Dupin et al. 2000; Avcı et al. 2019; Ramzan Parra et al. 2019), while the third component at 533 eV (in green) is related to weakly adsorbed oxygen species (Dupin et al. 2000). By observing

the evolution of the red component, it is possible to note that after the etching process, this component is enhanced, as in Figs. 3(c), (d), and (e). These results strongly suggest an increase in the density of defects of the material caused by the acid etching process. Table 4 summarizes the results of the O1s sub-peak component analysis.

Figure 4 displays the micrographs obtained from samples with different HCl etching times. It is possible to observe semispherical particles distributed over the entire surface of the material and also the presence of some elongated particles as the most bright features in the image of Fig. 4(a). After etching, two main features can be noted: (1) the average particle size decreases as the reaction occurs preferably in the grain boundaries, and (2) the film porosity increases as the acid promotes the formation of pores. Through ImageJ software (Schneider et al. 2012), it was possible to estimate the total area of the pores, resulting in 6.8% for the unetched sample, 17.4% for the sample etched during 10 to 26.8 s for the sample etched during 20 s, and 41.9% for the sample etched for 30 s.

Figure 5 shows the effect of thickness on the ozone sensing properties of ZnO unetched films. Comprehending the thickness impact on the gas sensing performance is extremely important because it can bring information on whether etching effects are only related to the thickness decrease caused by the acid or to the surface modification. Figure 5 presents the dynamic response-recovery curves of ZnO sensors prepared with thicknesses of 20, 50, 80, 220, and 500 nm. The response curves were measured under O$_3$ exposure cycles of 3 min. In this dataset, the O$_3$ concentration of each exposure cycle was 60, 120, 190, 250, and 300 ppb. The highest responses were observed for the sample with a thickness of 80 nm, as shown in Fig. 5(b).

Interestingly, the response decreases either for smaller or greater thicknesses, according to the lowest values observed for the 20- and 500-nm samples.

Table 2 Evolution of Raman A1 (LO) mode as a function of temperature

Raman modes			
Temperature (°C)	Peak 437 cm^{-1}	Peak 581 cm^{-1}	(*Peak*437/*Peak*581)100%
500	1142.37	125.93	11
600	702.45	66.32	9.4
700	1345.08	36.39	2.7

Fig. 3 XPS data of ZnO thin films as a function of etching time. **a**)Survey spectra and **b**, **c**, **d**, and **e** high-resolution O 1 s at etching times of 0, 10, 30, and 50 s, respectively. The high-resolution O 1 s region suggests that the etching procedure increases the O 1 s peak subcomponent related to defects in oxygen sites (red line)
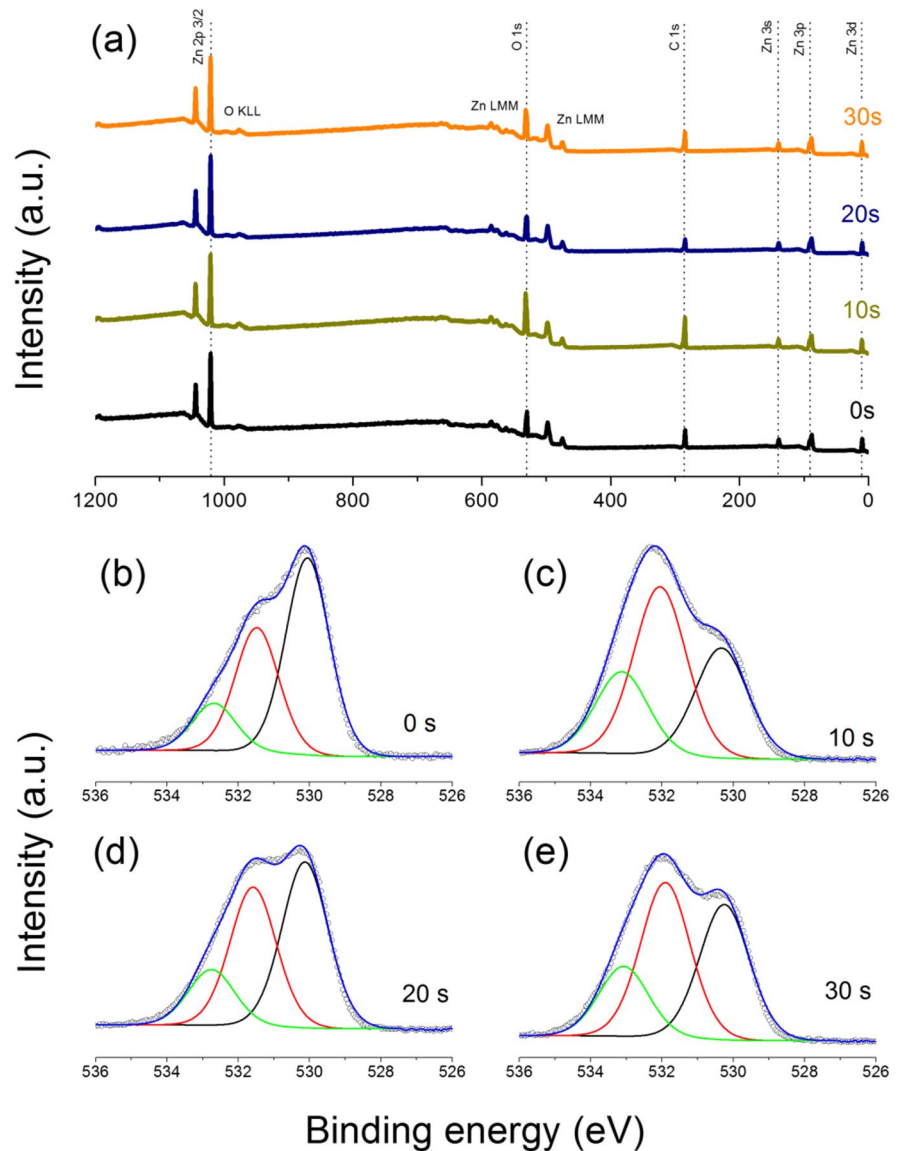
It is noticeable the existence of a correlation between film thickness, grain size, and porosity. When the thickness decreases, the grain size also decreases, increasing the surface area, favoring sensor sensitivity

Table 3 Survey XPS results of ZnO thin films prepared at different etching times

Etching time (s)	Surface composition (%)		
	Zn	O	C
0	10.8	32.6	56.6
10	5.7	32.37	61.93
20	12.8	40.3	46.92
30	8.3	35.5	56.2

Table 4 High-resolution XPS data for O 1 s for different etching times

Etching time (s)	High-resolution O 1 s sub-peak content (%)		
	Structural O (~ 530 eV)	Peroxide O^- (~ 532 eV)	Weakly adsorbed species (~ 533 eV)
0	10.8	32.6	56.6
10	5.7	32.4	61.9
20	12.8	40.3	46.9
30	8.3	35.5	56.2

Fig. 4 SEM micrographs of samples etched for **a** 0, **b** 10, **c** 20, and **d** 30 s. The images show two features that should impact the ZnO gas sensing properties: (1) it is possible to observe a decrease in the particle size, and (2) the formation of pores that could enhance the active surface area
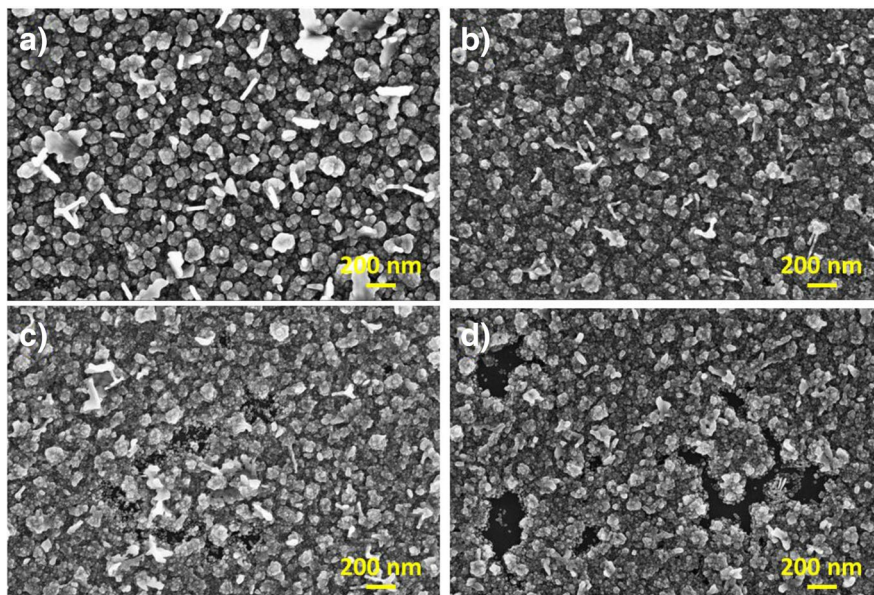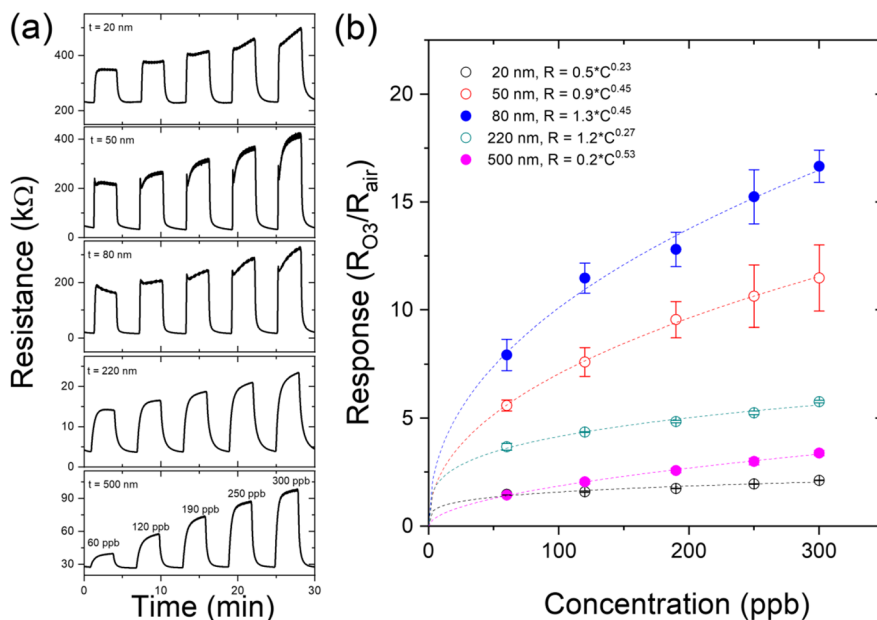

Fig. 5 Response of ZnO-based sensors prepared with different thicknesses. **a** Dynamic response-recovery curves for 20-, 50-, 80-, 220-, and 500-nm thicknesses. **b** Response as a function of O_3 concentration. These results suggest that the optimal relation between response and thickness lies in the vicinity of 80 nm

and shorter response and recovery times. These competing effects explain the dome-like behavior observed for the response vs. thickness curve, whose maximum was found to be in the vicinity of 80 nm, as seen in Fig. 5(b). This sample has a better correlation between grain size, thickness, and porosity.

Figure 6 presents a comparison of the sensing properties of the samples with thicknesses of 80,

220, and 500 nm before (in black) and after (in red) an HCl etching procedure for 30 s. It can be observed that all samples prepared with different thicknesses exhibited an increase in the maximum response value after the etching process, suggesting that the chemical etching effect is related to the decrease in the film thickness and the formation of surface pores. In these three conditions, the

Fig. 6 Dynamic response-recovery curves and response vs. O$_3$ concentration for samples with thicknesses of **a** and **b** 80 nm, **c** and **d** 220 nm, and **e** and **f** 500 nm. Etched samples exhibit a significant increase in their response towards ozone due to a higher active surface area
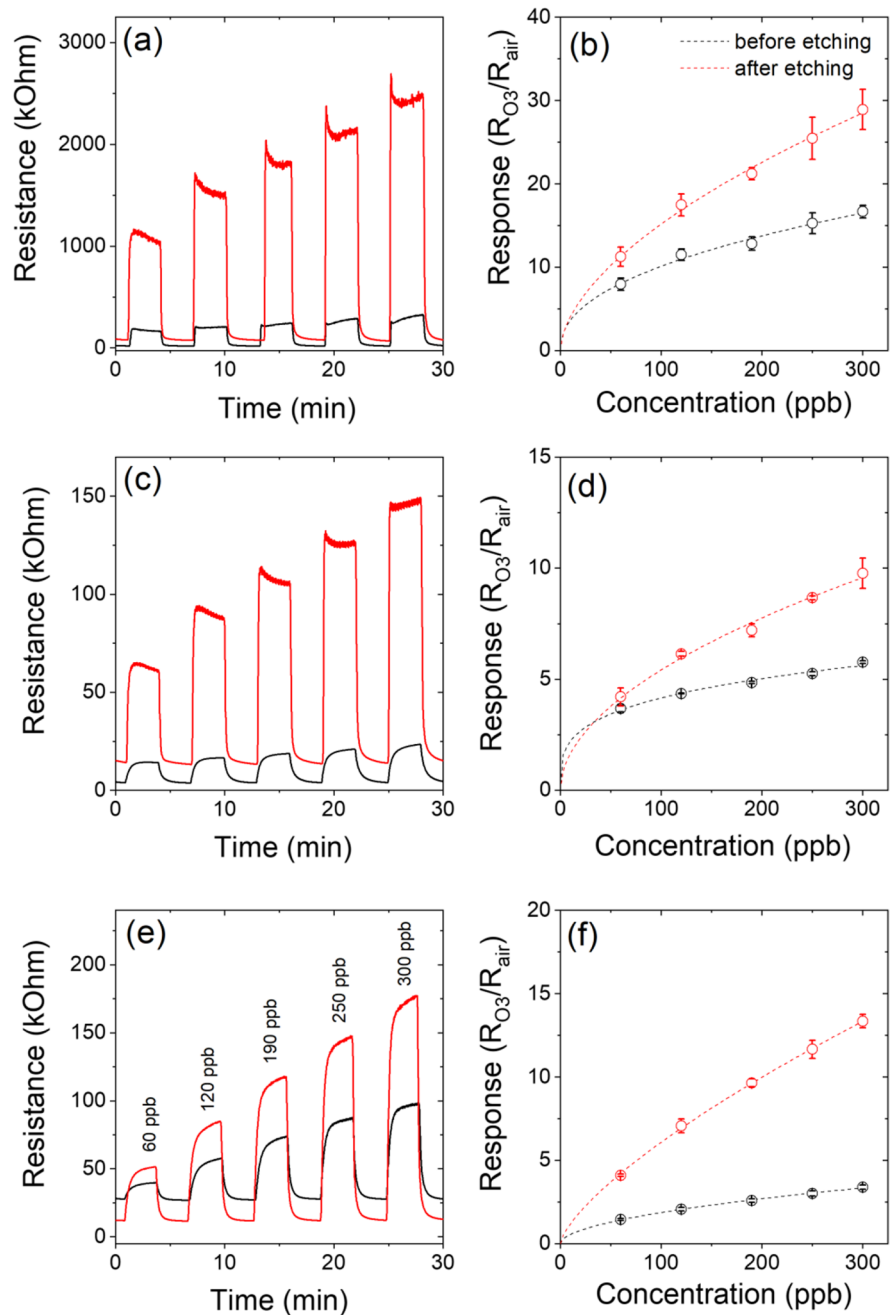
sensor response increased considerably, reaching a maximum in all samples after chemical etching, especially for the 80-nm sample, which presented the maximum response. The most significant relative increase in relation to the initial response was observed for the 500-nm sample. It can be explained by the larger average initial particle size compared to the other samples, which caused a greater increase in the final surface area than compared to the initial surface area. Figure 7 shows the effect of etching on the response and recovery times. It is possible to observe that only the response time of the 80-nm sample was not affected by the etching process, while the other two conditions exhibited a

Fig. 7 Comparison between response and recovery times of samples with thicknesses of **a** and **b** 80 nm, **c** and **d** 220 nm, and **e** and **f** 500 nm. Etched samples exhibit a significant decrease in their response time and recovery time towards ozone due to a microstructure with smaller particle sizes and the formation of pores
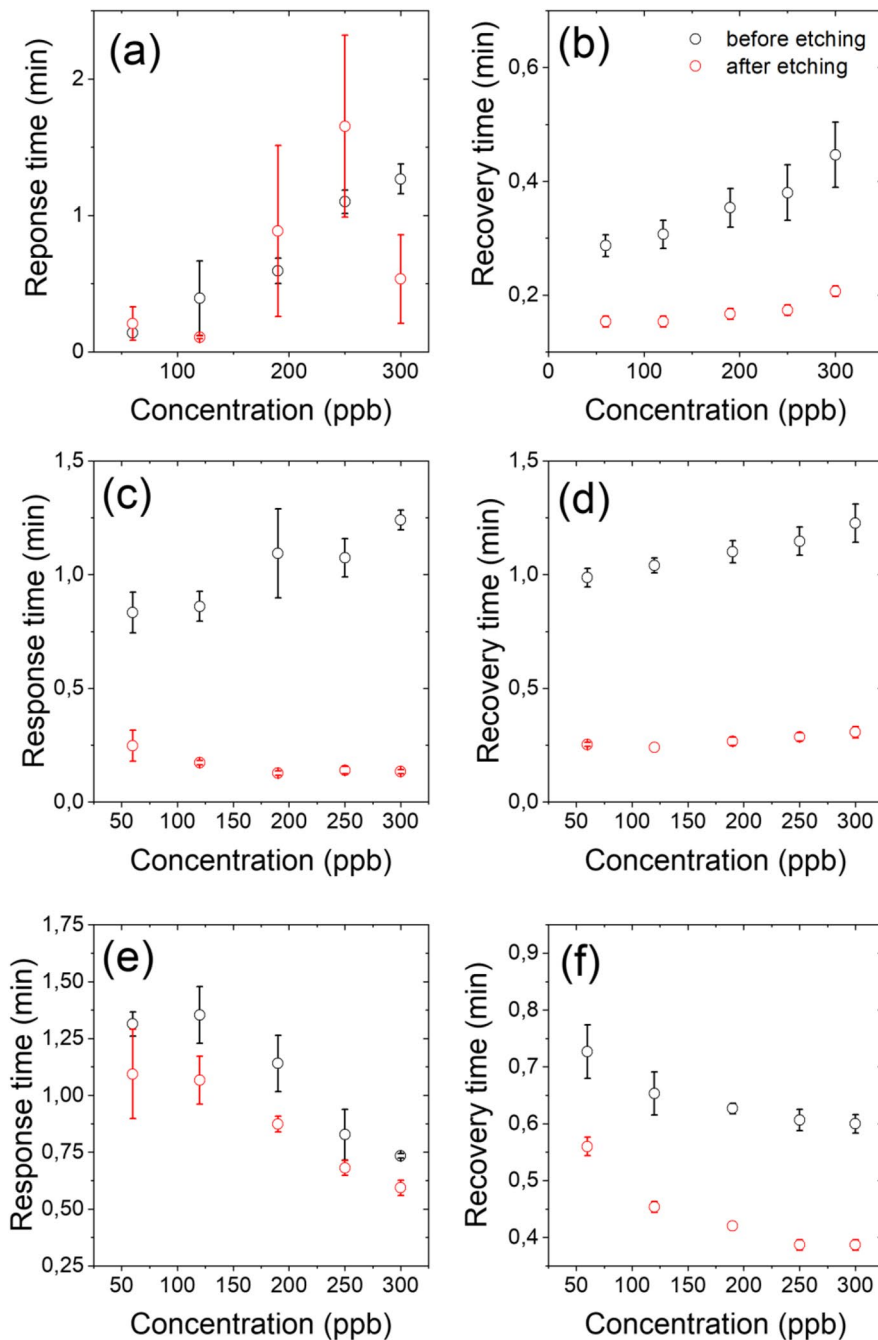
decrease in both the response and recovery times. It is worth mentioning that these two parameters, response and recovery times, are intimately correlated with the number of adsorption sites available on the material surface; that is, the higher the number of adsorption sites, the more O^- ions will be adsorbed within the same time. According to Yamazoe and Shimanoe (Yamazoe and Shimanoe 2008), the ozone adsorption process is the result of the following redox reaction:

$$O_{3(gas)} + e^-_{(surface)} \rightarrow O_{2(gas)} + e^-_{(surface)}$$
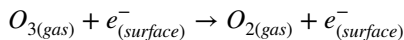
These results strongly suggest that HCl etching can improve the number of adsorption sites of ZnO, increasing its sensitivity and decreasing its response and recovery times.

Conclusions

This work presented a systematic study on the effect of HCl chemical etching on the surface morphology of ZnO thin films. The XPS data demonstrated that chemical etching could induce the formation of surface defects, providing a greater number of active gas adsorption sites. Regarding the effects on the microstructure, the SEM images showed that HCl etching decreases the mean grain size and induces the formation of pores, having a positive impact on the ozone-sensing properties of ZnO thin films with different thicknesses. This work opens perspectives for further studies on other SMOx and other studies regarding the influence of chemical etching on the selectivity of these materials towards other types of gases.

Data availability The datasets generated during and/or analyzed during the current study are available in the [Enhancement of the sensing properties through chemical-etched surface texturing] repository [Mendeley Data, V2, https://doi.org/10.17632/hxsfc3y75x.2].

Declarations

Conflict of interest The authors declare that they have no conflict of interest.

References

Aisida SO, Obodo RM, Arshad M, Mahmood I, Ahmad I, Ezema FI, Zhao TK, Malik M (2019) Irradiation-induced structural changes in ZnO nanowires. Nucl Instruments Methods Phys Res Sect B Beam Interact with Mater Atoms 458:61–71. https://doi.org/10.1016/J.NIMB.2019.07.041

Aisida SO Batool A Khan FM Rahman L Mahmood A Ahmad I Zhao T kai Maaza M Ezema FI 2020 Calcination induced PEG-Ni-ZnO nanorod composite and its biomedical applications. Mater. Chem. Phys. 255, 123603. https://doi.org/10.1016/J.MATCHEMPHYS.2020.123603

Avcı B, Caglar Y, Caglar M (2019) Controlling of surface morphology of ZnO nanopowders via precursor material and Al doping. Mater Sci Semicond Process 99:149–158. https://doi.org/10.1016/J.MSSP.2019.04.028

Barnard AS, Xiao Y, Cai Z (2006) Modelling the shape and orientation of ZnO nanobelts. Chem Phys Lett 419:313–316. https://doi.org/10.1016/j.cplett.2005.12.003

Barsan N, Koziej D, Weimar U (2007) Metal oxide-based gas sensor research: how to? Sensors Actuators, B Chem 121:18–35. https://doi.org/10.1016/j.snb.2006.09.047

Basyooni MA, Shaban M, El Sayed AM (2017) Enhanced Gas sensing properties of spin-coated Na-doped ZnO nanostructured films. Sci Rep 7:1–12. https://doi.org/10.1038/srep41716

Bunte E, Zhu H, Hüpkes J, Owen J (2011) Novel texturing method for sputtered zinc oxide films prepared at high deposition rate from ceramic tube targets. EPJ Photovoltaics 2:20602. https://doi.org/10.1051/epjpv/2011004

Catto AC, da Silva LF, Bernardi MIB, Li MS, Longo E, Lisboa-Filho PN, Nascimento OR, Mastelaro VR (2014) An investigation into the influence of zinc precursor on the microstructural, photoluminescence, and gas-sensing properties of ZnO nanoparticles. J Nanoparticle Res 16:1–9. https://doi.org/10.1007/s11051-014-2760-0

Cerqueira MF, Viseu T, De Campos JA, Rolo AG, De Lacerda-Aroso T, Oliveira F, Bogdanovic-Radovic I, Alves E, Vasilevskiy MI (2015) Raman study of insulating and conductive ZnO:(Al, Mn) thin films. Phys Status Solidi Appl Mater Sci 212:2345–2354. https://doi.org/10.1002/pssa.201532162

Colmenares YN, Correr W, Lima BS, Mastelaro VR (2020) The effect of morphology on the ozone-gas sensing properties of zinc oxide sputtered films. Thin Solid Films 703:137975. https://doi.org/10.1016/j.tsf.2020.137975

Dey A (2018) semiconductor metal oxide gas sensors: a review. Mater Sci Eng B 229:206–217. https://doi.org/10.1016/J.MSEB.2017.12.036

Dupin JC, Gonbeau D, Vinatier P, Levasseur A (2000) Systematic XPS studies of metal oxides, hydroxides and peroxides. Phys Chem Chem Phys 2:1319–1324. https://doi.org/10.1039/a908800h

Franco A, Pessoni HVS (2017) Effect of Gd doping on the structural, optical band-gap, dielectric and magnetic properties of ZnO nanoparticles. Phys B Condens Matter 506:145–151. https://doi.org/10.1016/j.physb.2016.11.011

Goldberger J, Sirbuly DJ, Law M, Yang P (2005) ZnO nanowire transistors. J Phys Chem B 109:9–14. https://doi.org/10.1021/jp0452599

Hu W Wan L Jian Y Ren C Jin K Su X Bai X Haick H Yao M Wu W 2018 electronic noses: from advanced materials to sensors aided with data processing. Adv Mater Technol 1800488. https://doi.org/10.1002/admt.201800488

Ji S, Ye C (2008) Synthesis, growth mechanism, and applications of zinc oxide nanomaterials. J Mater Sci Technol 24:457–472

Kong XY, Ding Y, Wang ZL (2004) metal-semiconductor Zn-ZnO core-shell nanobelts and nanotubes. J Phys Chem B 108:570–574. https://doi.org/10.1021/jp036993f

Korotcenkov G (2008) The role of morphology and crystallographic structure of metal oxides in response of conductometric-type gas sensors. Mater Sci Eng R Reports 61:1–39. https://doi.org/10.1016/J.MSER.2008.02.001

Luís F, Peko JM, Catto AC, Bernardini S, Mastelaro VR, Aguir K, Ribeiro C, Longo E (2017) Sensors and Actuators B : Chemical UV-enhanced ozone gas sensing response of ZnO-SnO 2 heterojunctions at room temperature. Sensors Actuators b Chem 240:573–579. https://doi.org/10.1016/j.snb.2016.08.158

Mahmud S, Abdullah MJ, Putrus GA, Chong J, Mohamad AK (2006) nanostructure of ZnO fabricated via French process and its correlation to electrical properties of semiconducting varistors. Synth. React. Inorganic. Met Nano-Metal Chem 36:155–159. https://doi.org/10.1080/15533170500524462

Matsuoka M (1971) Nonohmic properties of zinc oxide ceramics. Jpn J Appl Phys 10:736. https://doi.org/10.1143/JJAP.10.736

McCluskey MD Jokela SJ 2009: Defects in ZnO. J. Appl. Phys. 106. https://doi.org/10.1063/1.3216464

Nuss J, Wedig U, Kirfel A, Jansen M (2010) The structural anomaly of zinc: evolution of lattice constants and parameters of thermal motion in the temperature range of 40 to 500 K. Zeitschrift Für Anorg Und Allg Chemie 636:309–313. https://doi.org/10.1002/zaac.200900460

Owen JI, Hüpkes J, Zhu H, Bunte E, Pust SE (2011) Novel etch process to tune crater size on magnetron sputtered ZnO:Al. Phys Status Solidi Appl Mater Sci 208:109–113. https://doi.org/10.1002/pssa.201026164

Phan TL Vincent R Cherns D Nghia NX Ursaki VV 2008 Raman scattering in Me-doped ZnO nanorods (Me = Mn, Co, Cu and Ni) prepared by thermal diffusion. Nanotechnology. 19. https://doi.org/10.1088/0957-4484/19/47/475702

Ramzan Parra M, Pandey P, Siddiqui H, Sudhakar V, Krishnamoorthy K, Haque FZ (2019) Evolution of ZnO nanostructures as hexagonal disk: implementation as photoanode material and efficiency enhancement in Al: ZnO based dye sensitized solar cells. Appl Surf Sci 470:1130–1138. https://doi.org/10.1016/j.apsusc.2018.11.077

Ribeiro JM, Correia FC, Salvador PB, Rebouta L, Alves LC, Alves E, Barradas NP, Mendes A, Tavares CJ (2019) Compositional analysis by RBS, XPS and EDX of ZnO:Al,Bi and ZnO:Ga,Bi thin films deposited by d.c. magnetron sputtering. Vacuum 161:268–275. https://doi.org/10.1016/j.vacuum.2018.12.038

Rueden CT, Schindelin J, Hiner MC, DeZonia BE, Walter AE, Arena ET, Eliceiri KW (2017) Image J2: ImageJ for the next generation of scientific image data.

BMC Bioinformatics 18:529. https://doi.org/10.1186/s12859-017-1934-z

Russo V Ghidelli M Gondoni P Casari CS Li Bassi A 2014 Multi-wavelength Raman scattering of nanostructured Al-doped zinc oxide. J. Appl. Phys. 115. https://doi.org/10.1063/1.4866322

Savu R, Parra R, Joanni E, Jančar B, Eliziário SA, de Camargo R, Bueno PR, Varela JA, Longo E, Zaghete MA (2009) The effect of cooling rate during hydrothermal synthesis of ZnO nanorods. J Cryst Growth 311:4102–4108. https://doi.org/10.1016/j.jcrysgro.2009.06.039

Schneider CA Rasband WS Eliceiri KW 2012 NIH Image to ImageJ: 25 years of image analysis, https://www.nature.com/articles/nmeth.2089

Seiyama T, Fujiishi K, Nagatani M, Kato A (1962) A new detector for gaseous components using zinc oxide thin films. J Soc Chem Ind Japan 66:652–655. https://doi.org/10.1246/nikkashi1898.66.5_652

Shang C, Thimont Y, Barnabé A, Presmanes L, Pasquet I, Tailhades P (2015) Detailed microstructure analysis of as-deposited and etched porous ZnO films. Appl Surf Sci 344:242–248. https://doi.org/10.1016/j.apsusc.2015.03.097

Sopiha KV, Malyi OI, Persson C, Wu P (2021) chemistry of oxygen ionosorption on SnO2 surfaces. ACS Appl Mater Interfaces 13:33664–33676. https://doi.org/10.1021/ACSAMI.1C08236/SUPPL_FILE/AM1C08236_SI_001.PDF

Toby BH, Von Dreele RB (2013) GSAS-II: The genesis of a modern open-source all purpose crystallography software package. J Appl Crystallogr 46:544–549. https://doi.org/10.1107/S0021889813003531

Wang C, Yin L, Zhang L, Xiang D, Gao R (2010) Metal oxide Gas sensors: sensitivity and influencing factors. Sensors 10:2088–2106. https://doi.org/10.3390/s100302088

Yamazoe N, Shimanoe K (2008) Theory of power laws for semiconductor gas sensors. Sensors Actuators B Chem 128:566–573. https://doi.org/10.1016/j.snb.2007.07.036

Yan X, Venkataraj S, Aberle AG (2015) Wet-chemical surface texturing of sputter-deposited ZnO: Al films as front electrode for thin-film silicon solar cells. Int J Photoenergy 2015:1–10. https://doi.org/10.1155/2015/548984

Yan X Li W Aberle AG Venkataraj S 2016 Investigation of the thickness effect on material and surface texturing properties of sputtered ZnO:Al films for thin-film Si solar cell applications. https://doi.org/10.1016/j.vacuum.2015.10.027

Zhang R, Yin PG, Wang N, Guo L (2009) Photoluminescence and Raman scattering of ZnO nanorods. Solid State Sci 11:865–869. https://doi.org/10.1016/j.solidstatesciences.2008.10.016

Zhu L Zeng W 2017 Room-temperature gas sensing of ZnO-based gas sensor: A review.